Advances in
Geo-Energy Research

Vol. 14, No. 1, p. 34-48, 2024

Original article

Three-dimensional simulation of geologic carbon dioxide sequestration using MRST

Lluís Saló-Salgado[1,2], Olav Møyner[3], Knut-Andreas Lie[3], Ruben Juanes[1,2]*

[1]Department of Civil and Environmental Engineering, Massachusetts Institute of Technology, Cambridge 02139, United States
[2]Department of Earth, Atmospheric & Planetary Sciences, Massachusetts Institute of Technology, Cambridge 02139, United States
[3]Mathematics and Cybernetics, SINTEF Digital, Oslo 0373, Norway

---

Keywords:
Geologic carbon storage
MRST
open-source implementation
black-oil
relative permeability hysteresis

Cited as:
Saló-Salgado, L., Møyner, O., Lie, K. -A, Juanes, R. Three-dimensional simulation of geologic carbon dioxide sequestration using MRST. Advances in Geo-Energy Research, 2024, 14(1): 34-48.
https://doi.org/10.46690/ager.2024.10.06

Abstract:
Physics-based computational modeling of subsurface CO_2 migration constitutes the primary tool to assess geologic carbon storage. Such models are often required to plan injection operations and assess hazards such as CO_2 migration into units above the storage formation. Here, we present three tools developed to increase fidelity of black-oil type geologic carbon storage models in the open-source MATLAB Reservoir Simulation Toolbox. These tools, which are published in the `co2lab-mit` module, include functionality to: (1) Calculate and output PVT properties of miscible brine and CO_2 as a function of pressure, temperature, and salinity; (2) account for relative permeability hysteresis, necessary to model residual trapping; and (3) model CO_2 transport due to concentration gradients (molecular diffusion). We validate our implementation with published results including experimental observations, present `MRST` examples, and conclude with some remarks on applicability, limitations, and potential extensions. Source code and examples are provided.

---

1. Introduction

The MATLAB Reservoir Simulation Toolbox (`MRST`) (Lie, 2019; Lie and Møyner, 2021) is an open-source software that features multiple discretization schemes for simulating multiphase flow in porous media. Although not intended for full-fledged industrial use, the software includes many features and much of the functionality typically found in commercial simulators and workflow tools. `MRST` is well suited for rapid prototyping, thanks to the underlying interpreted language, powerful built-in functions, extensive numerical libraries, and efficient debugging tools offered by MATLAB. By also utilizing memory-optimized backends for linearization and assembly and high-end linear solvers implemented in a complied language (Lie and Møyner, 2021), `MRST` can be used to simulate both synthetic and real-life reservoir models with up to millions of unknowns. The toolbox has been extensively used to implement and validate novel models of subsurface flow in an industry-relevant environment (Landa-Marbán et al., 2021; Lie and Møyner, 2021; Wang et al., 2023). In terms of computational cost, `MRST` cannot fully compete with highly-optimized (and concurrent) simulators written in compiled languages, but it provides full access to all source code, can generate gradients and sensitivities with respect to variables and input parameters, and offers great flexibility in combining existing methods and models as well as implementing new ones.

`MRST` currently provides three main methods for simulating field-scale geologic carbon sequestration (GCS):

1) Vertical-equilibrium (VE) models (`co2lab-ve`) for analysis of structural trapping and long-term, large-scale migration assuming an instantaneous vertical equilibrium

Yandy Scientific Press

---

*Corresponding author.

E-mail address: lsalo@mit.edu (L. Saló-Salgado); olav.moyner@sintef.no (O. Møyner); knut-andreas.lie@sintef.no (K. -A. Lie); juanes@mit.edu (R. Juanes).

Received May 30, 2024; revised July 10, 2024; accepted August 18, 2024; available online August 20, 2024.

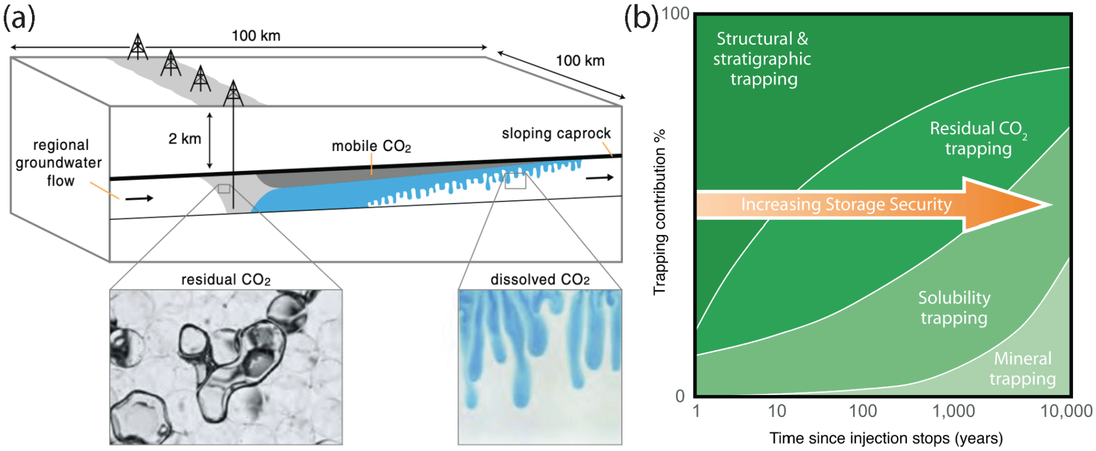

Fig. 1. Supercritical CO_2 trapping mechanisms. (a) Schematic of a sloping saline aquifer where CO_2 is injected through an array of wells. As mobile CO_2 migrates updip due to buoyancy (dark grey), brine imbibes at the trailing edge of the plume, immobilizing CO_2 blobs (see inset), and part of the CO_2 dissolves in brine, triggering a Rayleigh-Taylor instability where CO_2-rich brine sinks (see inset). From Szulczewski et al. (2012). And (b) contribution of different storage mechanisms as a function of time. Post CO_2 injection, the risk of CO_2 leakage decreases due to lower relative contribution of structural and stratigraphic trapping, with respect to the other three mechanisms. From Benson et al. (2005).

between brine and gas (Nilsen et al., 2015, 2016).

2) Full-scale solvers (such as `ad-blackoil` or `compositional`) for a more traditional approach to three-dimensional reservoir simulation (Landa-Marbán et al., 2021; Silva et al., 2023).
3) Multi-model approaches (`hybrid-ve`) that couple conventional 3D and upscaled models, including VE formulations (Møyner and Nilsen, 2019, 2020).

All three methods rely primarily on industry-standard finite-volume methods with implicit temporal discretization, two-point flux approximation, and single-point upstream mobility weighting.

The main advantage of VE models is computational efficiency, since they not only reduce the problem of CO_2 migration to two dimensions but also reduce numerical stiffness. This relaxes the requirements for detailed subsurface data, and can speed up computation by orders of magnitude. As a result, VE models are particularly useful for regional-scale studies and preliminary exploration or probabilistic assessments (Gasda et al., 2011; Szulczewski et al., 2012; Nilsen et al., 2016). Detailed analysis of well placement and CO_2 migration in a specific trap system, however, often requires dynamic simulations that honor subsurface heterogeneity and complex 3D structure.

The migration of a subsurface CO_2 plume is driven by the interplay of buoyancy and pressure gradients (Benson et al., 2005; Krevor et al., 2023) (Fig. 1). While buoyant CO_2 rises within the storage formation, it does not reach the surface due to trap systems including a caprock or top seal, faults bounding the storage system, and folds (structural and/or stratigraphic trapping) (Hesse and Woods, 2010; Saló-Salgado et al., 2024). Upon reaching the top of the formation or interbedded capillary barriers, the CO_2 plume spreads laterally and continues its gravity-driven migration updip in the formation, a process that can cover several kilometers and last hundreds of years or more, depending on geology (Gasda et al., 2011; Boait et al., 2012; Silva et al., 2023). As the plume migrates inside the storage formation, resident brine re-occupies pores previously filled with CO_2. This process, termed secondary imbibition, leads to CO_2 trapping in the form of blobs and ganglia when CO_2 saturation is low enough, known as residual or capillary trapping (Juanes et al., 2006). A fraction of the injected CO_2 will dissolve in the brine, leading to solubility or dissolution trapping. The aqueous mixture of saline water and CO_2 is denser than the resident brine and thuns sinks, thereby increasing storage security (Riaz et al., 2006; Hidalgo and Carrera, 2009; Neufeld et al., 2010; Szulczewski et al., 2012; Saló-Salgado et al., 2024). Finally, CO_2 can react with solid grains in the subsurface, which may precipitate carbonate minerals that permanently trap the CO_2 in solid phase (mineral trapping) (Benson et al., 2005). The first three mechanisms are active in sedimentary basins during operational timescales; the importance of mineral trapping depends on the composition of the trap system and typically increases with time (Benson et al., 2005; Krevor et al., 2023)(Fig. 1(b)).

The importance of different physical mechanisms in numerical simulation of CO_2 storage has been the subject of much research over the past two decades, and it is beyond the scope of this paper to summarize the state of the art at large. However, some relevant examples include Juanes et al. (2006), who showed that relative permeability hysteresis plays a major role in the migration of CO_2 in an anticline reservoir; Hidalgo and Carrera (2009) described accelerated CO_2 dissolution due to hydrodynamic dispersion; Saadatpoor et al. (2010) included local capillary heterogeneity within the injection layer, which led to inhomogeneous CO_2 rise and reduced invaded volume; Landa-Marbán et al. (2021) demonstrated that calcite precipitation leads to sealing of migration pathways; while Flemisch et al. (2024) and Saló-Salgado et al. (2024) compared multiple simulation models to experimental observations in a meter-scale laboratory setup, and showed that relatively small changes in PVT and multiphase flow properties can result in significantly different CO_2 migration. Outcomes from these studies and many others strongly suggest that a CO_2-brine system can be very sensitive to variations in subsurface properties and trapping mechanisms. Therefore, developing numerical models of GCS that include all relevant physics for a given geology and spatiotemporal scale is an important research area.

In this paper, we describe three extensions to the `MRST` automatic differentiation (AD) simulators, in particular the `ad-blackoil` module, developed to increase fidelity in simulation of 3D GCS. Specifically, Section 2 describes the implementation of a thermodynamic model to calculate PVT properties of CO_2-brine mixtures for black-oil simulators (Lie, 2019); Section 3 details the modeling of saturation-path-dependent relative permeability (hysteresis); and Section 4 provides an implementation of molecular diffusion. Lastly, in Sections 5 and 6 we present a practical case study and discuss the range of applicability and limitations of the models presented. Scripts and input files necessary to reproduce the examples presented in Sections 2, 3, 4, and 5 are available in the `co2lab-mit` module, distributed with `MRST` version 2024a or later.

It is important to note that the primary intent of the new module is to expand MRST's capabilities as a research tool to support the development of new models and computational methodologies, rather than to serve as a comprehensive tool for decision support in real-life operations. While it is capable of simulating large-scale storage operations, it does not achieve the full grid resolution that commercial simulators can offer. Consequently, the focus of our work is on facilitating innovation and exploration in GCS modeling, rather than delivering industrial-grade performance.

2. Generation of PVT data for black-oil models

Compositional reservoir simulators are widely used to accurately predict complex phase behavior in multicomponent models. In compositional simulation, equations of state (EoS) are employed to calculate the phase distribution and fluid properties in each grid cell. A black-oil simulator can be viewed as a specific, simple case of a compositional model with two or three pseudo-components, where miscibility properties are modeled as a function of pressure (P) changes only (Aziz and Settari, 1979; Lie and Møyner, 2021). Typically, the gas component can be present in either the oleic or gaseous phase, whereas the oil and water components exist only in their respective phases (Lie, 2019). To simulate GCS in CO_2-brine systems, the oleic phase can be set to represent brine[1], so that the main component in the gaseous phase (now CO_2) can dissolve in it. As shown below, it is also possible to consider vaporization of brine in the gaseous (CO_2) phase. Black-oil models often use tabulated input data to speed up calculations, and, due to their simplicity, can be significantly more efficient than general compositional models (Hassanzadeh et al., 2008).

In MRST, the `ad-blackoil` module (Lie, 2019) provides industry-standard reservoir simulation capabilities using black-oil models. For example, the module incorporates functionality for using external, pre-compiled linear solvers such as AMGCL (Lie, 2019; Lie and Møyner, 2021) and ECLIPSE-type input decks, and has been used to simulate GCS at spatial scales ranging from the laboratory to the field (Silva et al., 2023; Flemisch et al., 2024; Saló-Salgado et al., 2024). In this section, we summarize: (1) The implementation of a thermodynamic model for calculating CO_2-brine PVT properties; (2) the preparation of output data in ECLIPSE (SLB, 2014a) format, compatible with MRST's `ad-blackoil` module; and (3) usage in MRST. Our implementation follows the detailed description by Hassanzadeh et al. (2008), with a few modifications as described below.

2.1 Calculation of phase composition and PVT output

The composition of CO_2-brine mixtures is calculated based on the thermodynamic models presented by Duan and Sun (2003), Spycher et al. (2003), and Spycher and Pruess (2005), giving validity up to approximately 100 °C and 600 bar. Similar to Spycher and Pruess (2005) and Hassanzadeh et al. (2008), equilibrium relationships by Spycher et al. (2003) are used in combination with the activity coefficient formulation of Duan and Sun (2003) to determine the mole fractions of CO_2 and H_2O in the aqueous and gaseous phases, respectively. With this formulation, we can consider mixing between CO_2 and aqueous solutions of common species such as NaCl, KCl or $CaCl_2$, as well as seawater/brines. Our implementation of the solubility model and calculation of input quantities required for black-oil simulations (brine formation volume factor and gas-oil solution ratio) follows Hassanzadeh et al. (2008); this includes the assumptions of constant salinity and infinite dilution of H_2O in the gaseous phase to compute fugacity coefficients (Spycher et al., 2003), the Redlich-Kwong EoS (Redlich and Kwong, 1949) to compute gas molar volumes, Rowe Jr and Chou (1970) to compute brine density, Garcia (2001) to compute CO_2-saturated aqueous phase density, and Fenghour et al. (1998)'s model for CO_2 viscosity. Therefore, instead of repeating the lengthy formulation, we provide the code and validation figures (see Supplementary file), and note the following aspects of our implementation:

1) Given that CO_2 solubility in water is low, Hassanzadeh et al. (2008) considered that the salt mole fraction in the aqueous phase (x_{salt}) remains constant. We default to this option, but, as shown below, an option to include the effect of dissolved CO_2 can be used.
2) To calculate the density (ρ) of water-salt solutions (brine), a later correlation by Batzle and Wang (1992) can be used to expand the pressure (P), temperature (T) validity range (Rowe Jr and Chou (1970) is for $P < 350$ bar).
3) The dynamic viscosity (μ) of the aqueous phase accounts for CO_2 dissolution, in addition to P, T, and salinity (S). Similar to the density, we assume that the salinity effect on the aqueous phase viscosity can be modeled by considering a single salt species (NaCl), and use the

---

[1] For simplicity, we will refer to the oleic phase with brine properties assigned as the aqueous phase in the following text.

model presented by Islam and Carlson (2012).

4) As mentioned before, the dynamic viscosity of pure CO_2 is calculated using Fenghour et al. (1998) (we neglect the critical enhancement term). The viscosity of the gaseous phase (which may contain vaporized brine) is obtained via Davidson (1993)'s model for ideal gas mixtures; differences with respect to pure CO_2 are at most 2% for $T \in [30, 100]$ °C and $P \in [80, 400]$ bar. We note, however, that experimental viscosity data for supercritical CO_2-rich mixtures in the P, T range of interest was not found.

Although not our primary goal, vaporization of H_2O in the CO_2-rich phase is considered in the solubility model. Therefore, we can use similar arguments to those presented by Hassanzadeh et al. (2008) for the aqueous phase, and compute the vaporized oil-gas ratio (R_v) and gas formation volume factor (B_g) as follows:

$$R_v = \frac{V^s_{v\mathrm{H_2O}}}{V^s_{\mathrm{CO_2}}} = \frac{y_{\mathrm{H_2O}}\overline{\rho}^s_{\mathrm{CO_2}}}{\overline{\rho}^s_{\mathrm{H_2O}}y_{\mathrm{CO_2}}} \tag{1}$$

$$B_g = \frac{V^r_g}{V^s_{\mathrm{CO_2}}} = \frac{\rho^s_{\mathrm{CO_2}}}{\rho^r_g(1-v_{\mathrm{H_2O}})} \tag{2}$$

where V is volume, y is mole fraction in the gaseous phase, v mass fraction in the gaseous phase, $\overline{\rho}$ is molar density, and ρ is mass density; subscripts v and g refer to vaporized and gaseous phase, respectively; and superscripts s and r refer to standard conditions (defined here according to ECLIPSE (SLB, 2014a), i.e., 1 atm and 15.56 °C) and reservoir conditions, respectively. This means that, for instance, $\overline{\rho}^s_{\mathrm{CO_2}}$ denotes the molar density of the pure CO_2 phase at surface conditions, while ρ^r_g is the mass density of the gaseous phase at reservoir conditions, which in general will contain both CO_2 and H_2O. Because $y_{\mathrm{H_2O}}$ is at most 1%-2% at storage conditions, we consider $\rho_g \sim \rho_{\mathrm{CO_2}}$ and take $\rho_{\mathrm{CO_2}}$ from the Redlich-Kwong EoS. This simplification is reasonable based on available experimental data by King et al. (1992) and Hebach et al. (2004), who report changes smaller than experimental uncertainty for P up to 300 bar and T up to 60 °C. In the following, we will in most cases drop the superscript r, so that if no superscript is given, the quantity will be measured at reservoir conditions.

2.2 `MRST` example

The thermodynamic model described above is implemented in the function `pvtBrineWithCO2BlackOil`, which has the following syntax:

```
[t, rho_co2_s, rho_brine_s] = ...
pvtBrineWithCO2BlackOil(T, P, S, saltVar, ...
  vapH2O, unsatVals, figs);
```

Here, `T`, `P`, and `S` indicate the temperature, pressure range, and salinity, respectively. The boolean variables `saltVar`, `vapH2O`, `unsatVals` and `figs` indicate whether the change in salt mole fraction due to CO_2 dissolution into the brine should be accounted for, whether vaporized water should be considered, whether undersaturated values should be provided, and whether figures should be plotted, respectively. Variable outputs include a table `t` with all properties of interest for the gas and brine phase and the surface densities `rho_co2_s` and `rho_brine_s` of both phases at standard conditions. If `unsatVals` is set to `true`, a second table `t2` with undersaturated values can be requested. The function is well documented and interested users should refer to the code for full reference.

In `MRST`, fluid properties are specified by the fluid object, which tells the simulator which models should be used. In `ad-blackoil` models, the following properties need to be specified to model fluid PVT behavior (Lie, 2019): Surface densities ρ^s_α, formation volume factors B_α, and solution gas-oil ratio R_s, where α denotes a generic phase. Optionally, the vaporized oil-gas ratio R_v may be given if vaporization of brine into the gaseous phase is accounted for; see Section 2.1. Viscosities μ_α are also specified in the `fluid` object. As noted above, to simulate GCS in saline aquifers we assign brine properties to the oleic phase and CO_2 properties to the gaseous phase. The respective reservoir densities are computed as (Lie, 2019):

$$\rho_o = b_o(\rho^s_o + R_s\rho^s_g) \tag{3}$$

$$\rho_g = b_g(\rho^s_g + R_v\rho^s_o) \tag{4}$$

where we have introduced the reciprocal expansion and shrinkage factors $b_o = 1/B_o$ and $b_g = 1/B_g$, which are used by `MRST`, and ρ^s_α denote the densities of the respective phases at surface conditions.

The script `propertyTablesGenerationExample` details how to create a fluid object with all required PVT properties. To this end, we use the function `pvtBrineWithCO2BlackOil` to generate tabulated data suitable for an ECLIPSE-type input deck (SLB, 2014a). In this example, the input deck (`*.DATA` file) has already been prepared, and `MRST` will request download when the script is run for the first time. ECLIPSE deck files constitute the main input system in the `ad-blackoil` module (Lie, 2019). The fluid structure is then easily obtained:

```
% Read deck: fn is the .DATA file name
deck = convertDeckUnits(readEclipseDeck(fn));
% Generate fluid
fluid = initDeckADIFluid(deck);
```

Following Eqs. (3) and (4), we can recover phase densities as:

```
% Dry gas (no water)
rho_co2 = fluid.rhoGS*fluid.bG(p_val);
% Live oil (with CO2)
rss_val = fluid.rsSat(p_val);
rho_b_sat = fluid.bO(p_val,rss_val,true(np,1))
     .*(rss_val.*fluid.rhoGS + fluid.rhoOS);
rho_b = ...
  fluid.rhoOS*fluid.bO(p_val,zeros(np,1), ...
  false(np,1));
```

Here, `p_val` is an $n \times 1$ vector with the pressure values and `np` = n. Viscosities are obtained as:

```
mu_co2 = fluid.muG(p_val);
% CO2 saturated
mu_b_sat = ...
 fluid.muO(p_val,rss_val,true(np,1));
```

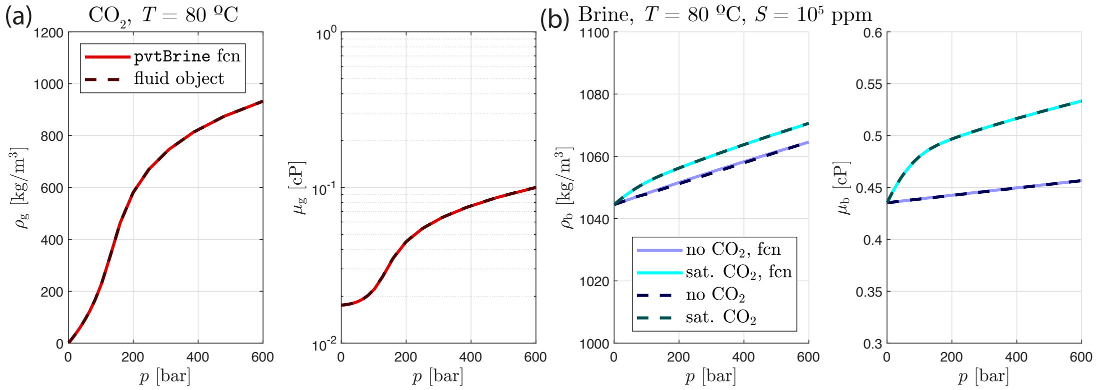

Fig. 2. Phase density and viscosity for (a) CO$_2$ and (b) brine, as computed from the `fluid` object (dashed lines, see main text) and the output of `pvtBrineWithCO2BlackOil` (solid lines). Vaporization was not considered in this example.

```
% No CO2
mu_b = ...
 fluid.muO(p_val,zeros(np,1),false(np,1));
```

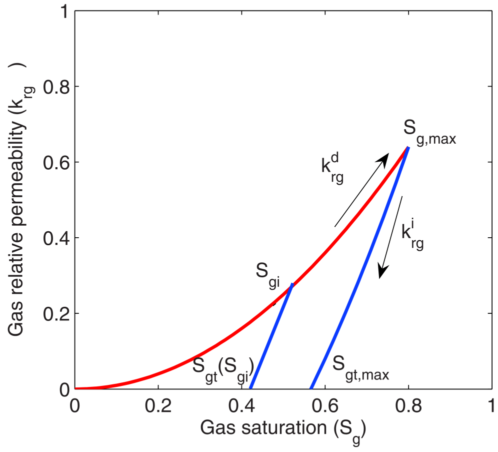

Fig. 3. Illustration of the primary drainage curve (red), bounding imbibition curve (to the right, blue) and scanning curve (in the middle, blue), as well as the Land's trapping model parameters (Land, 1968). Extracted from Juanes et al. (2006).

Fig. 2 shows the resulting phase densities and viscosities, where it can be seen that the values recovered from the `fluid` object are accurate to the tabulated output given by `pvtBrineWithCO2BlackOil`.

3. Relative permeability hysteresis

When multiple fluid phases are present in a porous medium, such as in GCS, the volumetric flux of a given phase ($\mathbf{u}_\alpha$, [L/T^1]) is given by the multiphase version of Darcy's law (Muskat, 1949):

$$\mathbf{u}_\alpha = -\frac{\boldsymbol{k} k_{r_\alpha}}{\mu_\alpha} (\nabla p_\alpha - \rho_\alpha \boldsymbol{g}) \tag{5}$$

where, $\boldsymbol{k}$ is the intrinsic permeability tensor [L^2], μ the dynamic viscosity [F/L^2·T], p the fluid pressure [F/L^2], ρ the mass density [M/L^3], $\boldsymbol{g}$ the gravity vector [L/T^2], and α indicates the fluid phase. $k_{r_\alpha}(S_\alpha) \in [0,1]$ is the relative permeability, a quantity introduced to account for the effect of multiple fluid phases in reducing the flow of a given phase α, depending nonlinearly on the saturation S_α (Muskat, 1949; Aziz and Settari, 1979). Due to pore-scale mechanisms, including contact-angle hysteresis and disconnection of the nonwetting phase during imbibition, relative permeability depends on the saturation path and saturation history, in addition to the current saturation (Juanes et al., 2006). In most subsurface aquifers, CO$_2$ will be the nonwetting phase (Awad and Espinoza, 2024); therefore, accounting for relative permeability hysteresis is necessary to accurately model CO$_2$ migration and trapping during GCS, especially during the post-injection stage (Juanes et al., 2006).

Relative permeability hysteresis models use a primary drainage and bounding imbibition curve to compute scanning curves in successive drainage and imbibition cycles, a process illustrated in Fig. 3 (Juanes et al., 2006). Several models have been described in the literature (Killough, 1976; Carlson, 1981; Spiteri et al., 2008), with reservoir simulators typically using either Killough's or Carlson's model for two-phase flow. Because there are two fluid phases during CO$_2$ storage in saline aquifers, in this work we use the model by Killough, following the implementation in ECLIPSE (Juanes et al., 2006; SLB, 2014b).

3.1 Killough's (1976) model

Consider the relative permeability of the nonwetting phase. Here, this is the CO$_2$-rich phase, which we refer to as the gaseous phase (subscript g). While the current saturation S_g is below the maximum historical saturation S_{gi}, the relative permeability along a scanning curve is computed as follows (Eq. (6), Fig. 3):

$$k^i_{rg}(S_g) = k^{ib}_{rg}(S^*_g) \frac{k^d_{rg}(S_{gi})}{k^d_{rg},(S_{g,\max})} \tag{6}$$

where k^{ib}_{rg} and k^d_{rg} refer to the bounding imbibition and drainage curves, respectively; $S_{g,\max}$ is the maximum gas saturation, i.e., one minus the irreducible water saturation; and S^*_g is the normalized saturation:

$$S^*_g = S_{gt,\max} + \frac{(S_g - S_{gt})(S_{g,\max} - S_{gt,\max})}{S_{gi} - S_{gt}} \tag{7}$$

Here, $S_{gt,\max}$ is the maximum trapped gas saturation associated with the bounding imbibition curve. The trapped gas saturation for the current scanning curve, S_{gt}, is computed based on Land's model (Land, 1968):

$$S_{gt} = S_{g,\min} + \frac{S_{gi} - S_{g,\min}}{1 + C(S_{gi} - S_{g,\min})} \tag{8}$$

where $S_{g,\min}$ is the minimum gas saturation along the primary drainage curve ($S_{g,\min} = 0$ in Fig. 3, to be consistent with the reservoir formation being saturated with brine before CO_2 injection). The Land trapping coefficient C is computed as:

$$C = \frac{1}{S_{gt,\max} - S_{g,\min}} - \frac{1}{S_{g,\max} - S_{g,\min}} \tag{9}$$

This model assumes that scanning curves are reversible, i.e., the same formulation is used during tertiary drainage as long as $S_g < S_{gi}$. As noted by Juanes et al. (2006), the bounding imbibition curve can be obtained from experiments, similar to the primary drainage curve, or following Land (1968). Killough (1976) also provided a model for hysteresis in the relative permeability of the wetting phase. However, because hysteresis effects in the wetting phase are usually less important (Juanes et al., 2006, and references therein), we limit this work to hysteresis effects in the nonwetting phase.

3.2 Implementation for use in `ad-blackoil`

Here, we summarize our implementation. This is provided to facilitate understanding as well as encourage extensions and modifications. Readers planning to use the current implementation via existing `*.DATA` input decks can directly skip to Section 3.3. Readers planning to modify `*.DATA` input decks or use alternative fluid property input methods should read Section 3.2.1 before moving to Section 3.3. Note that this implementation uses Killough (1976)'s model (Section 3.1) and is limited to gaseous phase relative permeability hysteresis (gas is assumed to be the nonwetting phase). Our implementation can be used with two-phase water-gas (immiscible) or oil-gas (miscible) black-oil models, for example in applications such as carbon dioxide or hydrogen storage. It can also be used in conventional, three-phase water-oil-gas black-oil models, but we note that hysteresis in the water-oil system requires an extension (see Section 6).

3.2.1 Input of hysteresis options

Typically, the hysteresis option is specified as part of an ECLIPSE input deck (i.e., a `*.DATA` file), which is the main input system in `ad-blackoil`; refer to Lie (2019) and SLB (2014a) for details, as well as the input decks for `relativePermeabilityHysteresisExample` discussed in Section 3.3. This requires adding the following to the input file:

1) The item `HYSTER` under the keyword `SATOPS` in the `RUNSPEC` section.
2) The keyword `EHYSTR` in the `PROPS` section. This keyword should be followed by a line with items `0.1 2 1.0 0.1 KR` terminated by `/`. In ECLIPSE, each of these items is used to specify different options for both capillary pressure and relative permeability hysteresis. In the present implementation, only items two and four are used: Item two indicates the hysteresis model, and therefore must be equal to 2 (Killough's model for the nonwetting phase). Item four is used in the implementation of Eq. (8) to improve convergence (Section 3.2.3), and should be 0.1 in most cases (default value).
3) Bounding imbibition curves using the appropriate keywords (`SWFN`, `SGFN`, `SGOF`, etc.), also in the `PROPS` section. Note that adding imbibition curves increases the number of saturation tables, so items under the keyword `TABDIMS` in the `RUNSPEC` section may need to be updated.
4) The `IMBNUM` keyword in the `REGIONS` section, followed by a set of lines specifying the cells pertaining to each imbibition region. Alternatively, this can also be added manually to the `rock` object, as shown shortly.

The example described in Section 3.3 uses the `CASE2.DATA` input deck, provided by Juanes et al. (2006), where these options are used. The `fluid` object is generated as shown in Sections 2.2 and 3.3, which will automatically add the flag `fluid.krHyst=1`, indicating that hysteresis is active in all cells (all model regions). If hysteresis is desired in a subset of model regions only, `krHyst` should be modified with an array of size $1 \times n$, in which each entry is an imbibition region number (corresponding to the unique values in `rock.regions.imbibition`) where hysteresis is active.

Alternatively, if the `fluid` and `rock` objects (Lie, 2019) are generated without an input deck, hysteresis options and flags can be added manually, for instance:

```
fluid.ehystr = {0.1, 2, 1, 0.1};
% 1 (all) or subset of imb regions for
   hysteresis
fluid.krHyst = 1;
nreg = max(rock.regions.saturation);
rock.regions.imbibition = ...
  rock.regions.saturation + nreg;
```

Hysteresis can also be deactivated in any given run by removing the field `krHyst` or setting it to zero.

3.2.2 Code structure and location

The implemented changes can be subdivided in the following two groups:

1) Input deck processing. This refers to changes needed to read `*.DATA` input decks with hysteresis specifications (i.e., the `EHYSTR` keyword in the `PROPS` section).
2) Creation of a new flow-property state function to evaluate the hysteretic relative permeability function, called `HystereticRelativePermeability`.

Accordingly, the code is implemented in the corresponding MRST modules:

1) `deckformat`: A new case `'EHYSTR'` is added within the function `readPROPS`. This enables `assignEHYSTR` (in the `ad-props` module) to handle the `EHYSTR` keyword in the input deck.

2) `ad-props`: The function `assignEHYSTR`, called under `initDeckADIFluid`, assigns hysteresis options and flags to the `fluid` object (example in Section 3.3). The flag `fluid.krHyst` will be automatically set to 1 (hysteresis active in all cells) if hysteresis is requested in the input deck. As described in Section 3.2.1, this flag can be modified to limit hysteresis to a region subset.
3) `ad-core`: Hysteretic relative permeabilities are handled by the state function `HystereticRelativePermeability` (Lie, 2019; Lie and Møyner, 2021). This class incorporates the following:
    - The function `addScanKr` computes scanning curves. As noted above, this currently uses Killough's model and is limited to gaseous phase relative permeability. A slight modification to Killough's model is added to improve convergence, as described in Section 3.2.3.
    - The method `evaluatePhaseRelativePermeabilityWithHysteresis` checks for the `krHyst` flag in the fluid object and uses the appropriate relative permeability model where hysteresis is active. This is currently limited to the gaseous phase.

3.2.3 Modifications and safeguards

Our implementation within `addScanKr` uses a modification to Eq. (8), introduced to improve convergence as done in ECLIPSE (SLB, 2014b):

$$S_{gt} = S_{g,\min} + \frac{S_{gi} - S_{g,\min}}{A + C(S_{gi} - S_{g,\min})} \tag{10}$$

where $A = 1 + a(S_{g,\max} - S_{gi})$. ECLIPSE uses a default value of $a = 0.1$ (SLB, 2014b), but the user can specify a different value as described in Section 3.2.1. The function `addScanKr` also ensures the following:

- That the imbibition curve lies below the drainage curve, $k^i_{rg}(S_g) \leq k^d_{rg}(S_g)$.
- The minimum tolerance for flow reversal was set to 10^{-3}. This means that unless $S_g + 10^{-3} < S_{gi}$, the drainage curve is used.
- Unless $S_{gi} > S_{gh} + S_{g,\min}$, the drainage curve is always used, where S_{gh} is defaulted to 0.05, but can be updated by the user as shown in Section 3.3.

3.3 MRST example: Validation with the PUNQ-S3 model

We validate our implementation using the PUNQ-S3 geologic model example that represents a three-dimensional reservoir with heterogeneous permeability and anticlinal structure. Juanes et al. (2006), who provide additional details, used an adapted version of this model to elucidate the impact of relative permeability hysteresis on GCS, which we reproduce. The model has 1,761 active cells and represents a good compromise between a lightweight setup that can be run quickly on a standard laptop, and a realistic storage aquifer. CO_2 injection is conducted over a ten-year period from eight wells operating at a reservoir volume rate of 18 rm^3/day each. After the initial 10 years, CO_2 migration continues until year 500. In this example, CO_2 and water are considered immiscible. A detailed description of this case is provided by Juanes et al. (2006).

Complete source code for the example can be found in the script `relativePermeabilityHysteresisExample`. Here, we only show the key statements to run this model with nonwetting phase relative permeability hysteresis. First, the `fluid` structure is generated using the input deck:

```
fn = fullfile(getDatasetPath('co2labmit'), ...
  'punq-s3', 'CASE2.DATA');
deck = convertDeckUnits(readEclipseDeck(fn));
fluid = initDeckADIFluid(deck);
% imb reg where hysteresis is active
fluid.krHyst = 2;
```

In this case, there is a single fluid region containing all active cells. Therefore, `rock.regions.saturation = ones(G.cells.num, 1)`. Here, the field `rock.regions.imbibition` is directly assigned to the `rock` object using the input deck. The model and relative permeability state function are defined as:

```
% Use deck to select model
model = selectModelFromDeck(G, rock, ...
  fluid, deck);
% Set up the state function groups
model = model.validateModel();
% Update relperm state function
model.FlowPropertyFunctions = ...
model.FlowPropertyFunctions.setStateFunction(
  'RelativePermeability', ...
HystereticRelativePermeability(model));
% optional (defaults to 0.05)
model.FlowPropertyFunctions.
    RelativePermeability.minSat = 0.02;
```

Once the model setup is complete, we run the simulation using `simulateScheduleAD` or `simulatePackedProblem` (Lie, 2019). Fig. 4 compares our solution with results presented by Juanes et al. (2006), which were obtained with the commercial simulator ECLIPSE 100 (SLB, 2014a), and shows excellent agreement between the two models.

4. Molecular diffusion

When $n > 1$ components are present in a fluid phase, concentration gradients will result in transport of molecules from regions of higher concentration to regions of lower concentration. Accordingly, the total macroscopic flux will be given by the sum of the advective flux associated with the movement of the fluid phase and the diffusive flux associated with molecular transport within the fluid phase (Bear, 1972). Typically, molecular diffusion between components is not accounted for in black-oil models (Lie, 2019); as we show shortly, this is justified given the magnitude of numerical diffusion, compared to its physical counterpart, in field-scale models. In certain cases, however, it may be necessary to include diffusive fluxes to obtain accurate simulations. An example of this is the validation of numerical models with centimeter- to meter-scale experimental results, which require

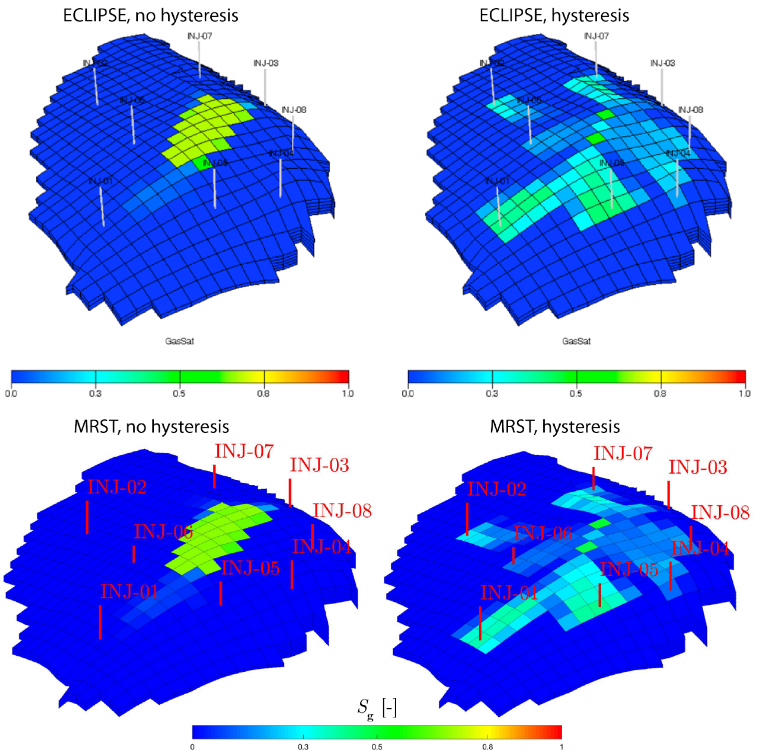

Fig. 4. CO_2 saturations after 500 years. The top row results are from Juanes et al. (2006) (obtained using ECLIPSE 100). Bottom results are with the described implementation in `MRST`. The left column shows results for Case 1 (no hysteresis), while the right column shows results for Case 2 (hysteresis).

higher resolution due to the smaller spatial scales involved (Saló-Salgado et al., 2024).

First, we provide the mathematical model for the diffusive mass flux of a solute in porous media and briefly discuss the contrasts between physical and numerical diffusion (Section 4.1). Next, we summarize our implementation of molecular diffusion of CO_2 in brine for use in `ad-blackoil` (Section 4.2), and, finally, we present a full `MRST` example (Section 4.3).

4.1 Mathematical model

Consider a generic multiphase, multicomponent fluid system. The mass conservation equations for each component $\gamma = 1, \ldots, M$ can be written as (Lie, 2019):

$$\frac{\partial}{\partial t}\left(\phi \sum_{\alpha} \rho_\alpha S_\alpha \chi_\alpha^\gamma\right) + \nabla \cdot \left(\sum_{\alpha} \mathbf{J}_\alpha^\gamma\right) = Q^\gamma \tag{11}$$

where ϕ is the porosity, α denotes a generic fluid phase, S is the saturation, χ_α^γ the mass fraction of component γ in phase α, and Q^γ is a total mass term for component γ, including wells. The total macroscale flux $\mathbf{J}$ can be decomposed as (Bear, 1972, 2018):

$$\mathbf{J}_\alpha^\gamma = \mathbf{J}_{\alpha,\mathrm{adv}}^\gamma + \mathbf{J}_{\alpha,\mathrm{dif}}^\gamma \tag{12}$$

i.e., as a sum of advective and diffusive fluxes, respectively, which can be written as (Bear, 1972; Lie, 2019):

$$\begin{aligned} \mathbf{J}_{\alpha,\mathrm{adv}}^\gamma &= \rho_\alpha \chi_\alpha^\gamma \mathbf{u}_\alpha \\ \mathbf{J}_{\alpha,\mathrm{dif}}^\gamma &= -\rho_\alpha S_\alpha \mathbf{D}_\alpha^\gamma \nabla \chi_\alpha^\gamma \end{aligned} \tag{13}$$

where, $\mathbf{D}_\alpha^\gamma$ is the total diffusion coefficient (L^2/T), which is a second-order tensor that can can be further decomposed into a coefficient $\mathbf{D}_{\alpha,m}^\gamma$ of molecular diffusion and a coefficient $\mathbf{D}_{\alpha,h}^\gamma$ of hydrodynamic dispersion

$$\mathbf{D}_\alpha^\gamma = \mathbf{D}_{\alpha,m}^\gamma + \mathbf{D}_{\alpha,h}^\gamma = \phi \mathscr{D}_{\alpha,m}^\gamma \mathbf{T}_\alpha + \mathbf{D}_{\alpha,h}^\gamma \tag{14}$$

where ϕ is porosity, $\mathscr{D}_{\alpha,m}^\gamma$ a scalar molecular diffusivity (L^2/T), and $\mathbf{T}_\alpha$ a dimensionless tortuosity tensor.

Note that Eq. (14) assumes a Fickian model (Fick, 1855) for both the diffusive and dispersive components (i.e., the flux is driven by a concentration gradient). Hydrodynamic dispersion is introduced to explain increased macroscale spreading observed in non-stagnant fluids in porous media, and multiple models have been proposed; see Bear (2018) and references therein. Tortuosity is a geometrical quantity that accounts for the path length of extensive quantities in porous media being longer than the Euclidean distance, and it is a tensorial quantity in anisotropic media. Because $\mathbf{T}_\alpha$ depends on the specific configuration of the porous medium, it is best determined experimentally (Bear, 2018). Hence, for simplicity, we limit the present implementation to a scalar diffusion coefficient, i.e., a pseudo-diffusivity (D_α^γ):

$$\mathbf{J}_{\alpha,\mathrm{dif}}^\gamma = -\phi \rho_\alpha S_\alpha D_\alpha^\gamma \nabla \chi_\alpha^\gamma \tag{15}$$

In our two-phase model of CO_2 and brine, $D_\alpha^\gamma = D_o^{CO_2}$ with o denoting the oleic phase (assigned properties of brine).

In dilute aqueous solutions, $\mathscr{D}_{\alpha,m}^\gamma \sim \mathscr{O}$ (10^{-9}) m^2/s, with $\mathscr{D}_{\mathrm{brine}}^{CO_2}$ of the order 2-3 $\times 10^{-9}$ at 40 °C and of the order

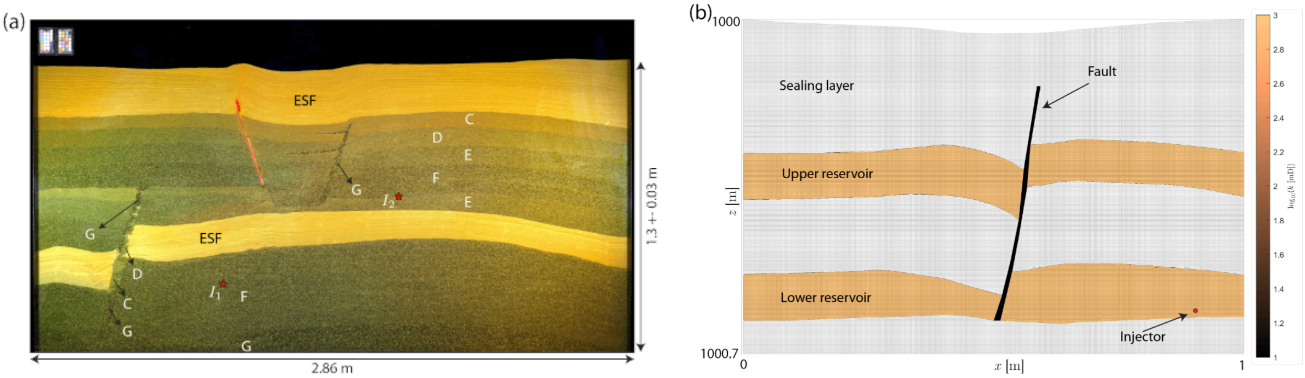

Fig. 5. A test case derived from the FluidFlower experiment. (a) Overview of the porous medium used in the original international benchmark study (Flemisch et al., 2024). Letters indicate different sand types, and three fault structures are present. Modified from Saló-Salgado et al. (2024). And (b) setup used herein to illustrate the effect of CO_2 diffusion on convective fingers, repositioned at 1 km depth. $h \approx 2.5$ mm. The colormap shows reservoir and fault permeability (1 D and 10 mD, respectively).

4-5 $\times 10^{-9}$ at 80 °C, respectively (Al-Rawajfeh, 2004). For the numerical diffusion, we have that $D_{\text{num}} \sim uh$, where h is the cell size. For illustration purposes, let us consider a porous formation at storage depth. Taking permeability $k = 100$ mD, viscosity $\mu = 0.8$ cP, and a modest pressure gradient $\nabla p = 10$ mbar/m (for $\Delta p = 1$ bar in 100 m), $u \approx 1.2 \times 10^{-7}$ m/s (via Darcy's law). In a typical reservoir-scale model, $h \sim \mathscr{O}(10^1\text{-}10^3)$ m, which gives $D_{\text{num}} \sim \mathscr{O}(10^{-6}\text{-}10^{-4})$ m^2/s. Therefore, it is evident that physical diffusion is negligible at this scale. If we now consider the FluidFlower rig (Fernø et al., 2024; Haugen et al., 2024) as an example of a laboratory setup at the meter scale, $h \sim 10^{-3}$ m. In this setup, Saló-Salgado et al. (2024) estimated numerical diffusion to be comparable to or smaller than physical diffusion almost everywhere in their simulations; hence, some degree of diffusivity needs to be introduced if one wants to perform both lab-scale and field-scale simulations.

4.2 Implementation for use in `ad-blackoil`

Our implementation is directed towards models that are set up using the `GenericBlackOilModel` class, and simply adds a diffusive component to the total flux term (which, by default, is just the advective flux). Similar to the implementation of relative permeability hysteresis described in Section 3, where we update the relative permeability state function, here we modify the state function for the total CO_2 flux (Lie and Møyner, 2021). To do this, the user simply needs to specify the pseudo-diffusivity and update the `ComponentTotalFlux` using `CO2TotalFluxWithDiffusion` (as shown in Section 4.3).

The key statements within the evaluation method in the class `CO2TotalFluxWithDiffusion` are provided below. Note that some of these have been simplified for readability, so interested users should refer to the actual code for full details:

```
% 1. Get quantities
% Model operators;
op = model.operators;
% Face diffusivity (analogous to
   transmissibility)
T = getFaceDiffusivity(model.G, model.rock);
% Get mass fraction of CO2
X_co2 = MassCo2InBrine ./ massBrine;
% Get molecular diffusivity and update T
C = prop.componentDiffusion;
Tc = C(2).*T;
% Mass fraction gradient
grad_xi = op.Grad(X_co2);
% Face density and saturation according to
   centered or upwind scheme
if faceAvg, ..
else, ..; end

% 2. Get diffusive flux and update total flux
% kg/s/m^2
diff_flux = -faceDens.*faceS.*Tc.*grad_xi;
% Update total CO2 flux
v{2} = v{2} + diff_flux;
```

We emphasize that the `GenericBlackOilModel` class uses mass fluxes instead of surface volumes (used by the earlier, specific black-oil model classes such as `ThreePhaseBlackOilModel`). This ensures consistent units between solvers and facilitates model management. We also note that a code structure similar to the one described here, with a class that incorporates the desired flux model, can be used to extend this implementation (Lie and Møyner, 2021).

4.3 `MRST` example: The effect of CO_2 diffusion on convective fingers

To illustrate the effect of adding CO_2 diffusion in brine, we present an example inspired by recent work on the FluidFlower project (Eikehaug et al., 2024; Fernø et al., 2024; Flemisch et al., 2024; Haugen et al., 2024; Saló-Salgado et al., 2024). The FluidFlower is a meter-scale, quasi-2D experimental rig with transparent panels. It can be filled with sands to create realistic cross sections, and multiple ports provide capabilities for multiphase/multicomponent injection and monitoring (Fig. 5(a)).

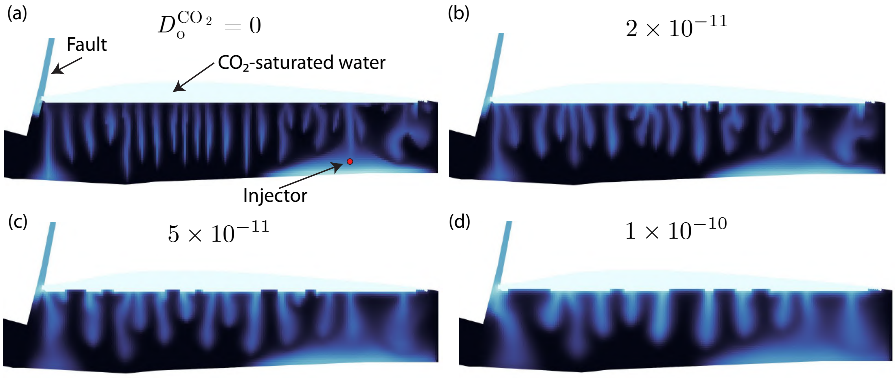

Fig. 6. Overview of convective mixing in the lower right reservoir using different pseudo-diffusivities: (a) No diffusion, (b) $D = 2 \times 10^{-11}$ m^2/s, (c) $D = 5 \times 10^{-11}$ m^2/s, and (d) $D = 1 \times 10^{-10}$ m^2/s. Grid cell size $h \approx 2.5$ mm. Note that the average spacing and finger width increases with the diffusivity.

We generated a simple stratigraphic section with dimensions $0.01 \times 1 \times 0.66$ meters, including a fault structure, and set it at a depth of 1 km. At this depth, CO_2 is in a supercritical state, which is the intended condition for storage in sedimentary basins. Compared to the FluidFlower, which operates at surface conditions, this setup facilitates the convergence of the nonlinear solver. The primary reason is that CO_2 is significantly more buoyant at surface conditions, where it exists in a gaseous state (Saló-Salgado et al., 2024). The reservoir and fault permeability can be seen on top of the grid ($h \approx 2.5$ mm) in Fig. 5(b). We inject CO_2 into the lower right of the domain at a surface rate of 8 ml/min during one day, and run the simulation for 30 days.

This example is provided in the script `flowWithDiffusionExample`. We specify two phases, oil (with properties of water) and gas. The model can be set up using `GenericBlackOilModel` and `CO2TotalFluxWithDiffusion`:

```
% Create model (oil is water)
model = GenericBlackOilModel(G,rock,fluid, ...
        'disgas',true,'water',false);
% Add state function groups
model = model.validateModel();
% Specify diffusion
% scalar pseudo-diffusivity for CO2 in water
D = 1e-10;
diff_flux = CO2TotalFluxWithDiffusion(model);
% water in gas phase not considered
diff_flux.componentDiffusion = [0 D];
% Centered scheme
diff_flux.faceAverage = true;
% Update model
model.FlowDiscretization.ComponentTotalFlux =
    diff_flux;
```

Note that the value of $D_o^{\mathrm{CO}_2}$ may need to be smaller than the molecular diffusivity $\mathscr{D}_o^{\mathrm{CO}_2}$, depending on the magnitude of advective fluxes and grid resolution. Fig. 6 compares convective fingers after CO_2 injection in the lower-right reservoir, using different $D_o^{\mathrm{CO}_2}$ values. It is evident that the finger thickness and spacing change as diffusive fluxes are introduced in the system; as noted earlier, this may be required in meter-scale or smaller setups, for example to history-match simulation models to experiments that provide a ground truth (Saló-Salgado et al., 2024).

5. Practical case study: CO_2 injection in the Johansen formation, North Sea

So far, we have validated our implementation through several specific cases:

1) We have compared our calculations of phase composition and various PVT properties against results reported in the literature, including experimental data not used in developing our equations (see Supplementary file).
2) The PUNQ-S3 model in Section 3.3 validated relative permeability hysteresis.
3) The FluidFlower example in Section 4.3 validated molecular diffusion.

Additionally, we note that Saló-Salgado et al. (2024) provide detailed studies of the original FluidFlower experiments on a grid with 150,000 cells, using all three developments discussed in more detail herein; additional simulation results are found in Haugen et al. (2024). The FluidFlower project has subsequently led to the 11th Society of Petroleum Engineers Comparative Solution Project (Nordbotten et al., 2024), which addresses simulation challenges associated with CO_2 storage operations. Similarly, Silva et al. (2023) present a 3-million cell CO_2 simulation on a representative field-scale geological model in the Gulf of Mexico, also utilizing the thermodynamic and relative permeability hysteresis models described here.

Therefore, instead of presenting a new real-life application, we describe here a conceptual study that focuses more on the practical usage and computational aspects of `MRST`. This case is provided in the script `co2JohansenExample`, which contains the following:

1) Usage and visualization of corner-point grids and petrophysical properties.
2) Generation of PVT properties according to reservoir depth and setup of saturation functions.
3) Definition of a CO_2 injection well with specific mass flow rate.

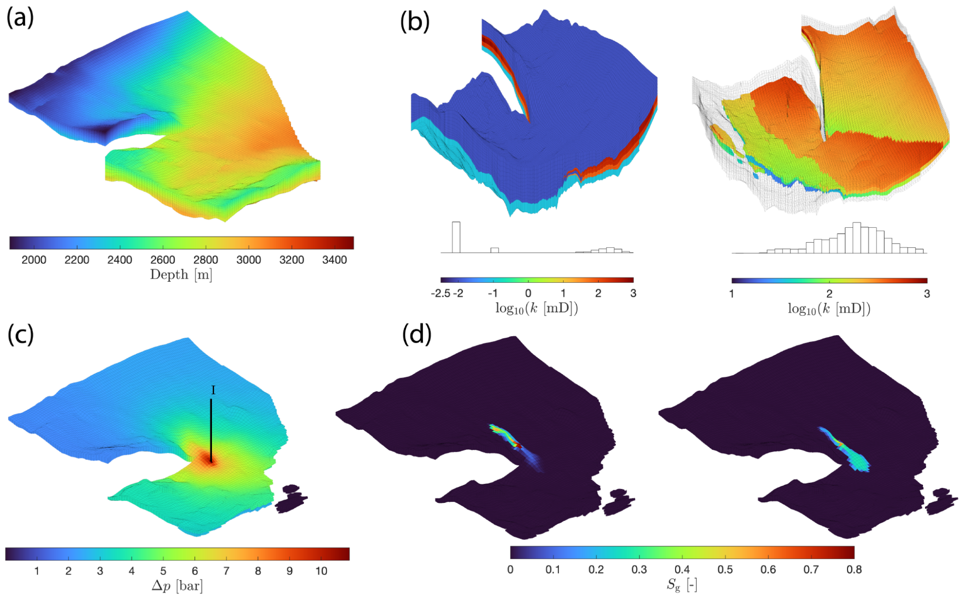

Fig. 7. Overview of CO_2 injection in the Johansen Formation. (a) Depth map of the reservoir simulation model, (b) horizontal permeability map for all cells (left), and the subset of cells corresponding to the Johansen sand (right). Note the histograms reported above the colorbar, (c) well location and pore pressure increase in the Johansen sand at the end of CO_2 injection ($t = 30$ years) and (d) CO_2 saturation in the Johansen sand at the end of the simulation period ($t = 500$ years), without (left) and with (right) relative permeability hysteresis.

4) Activation or deactivation of relative permeability hysteresis.
5) Visualization of simulation results.
6) Computation of performance metrics.

We selected the Johansen formation, a sandstone saline aquifer located offshore the west coast of Norway at 2-3 km depth (Fig. 7(a)), as it is a possible candidate for CO_2 injection. We employ a public $100 \times 100 \times 11$ corner-point grid model with 90,000 active cells, representing a small but realistic cell count for a reservoir simulation model. The horizontal extent of the model is about 50 km in both x and y axes. Further details are given by Lie (2019). The simulation model includes, from bottom to top, the Amundsen shale, the Johansen sand, and the Dunlin shale, with one, five, and five layers of cells, respectively. The horizontal permeability (k) of the Johansen sand is between 10 and 900 mD (Fig. 7(b)).

The accompanying script `co2JohansenFluidProps` provides the fluid properties (PVT and saturation functions). We note that these properties were selected for the purposes of this conceptual example only and are not necessarily representative of the actual properties of the Johansen sand. The CO_2 injection well is located at the center of the model and controlled by constant rate (Fig. 7(c)). We inject 1 Megatonne of CO_2 per year during the first 30 years and continue to run the simulation for another 470 years after the injection ceases, giving a total simulation period of 500 years. This represents a realistic volume and time frame for industrial-scale CO_2 sequestration (Silva et al., 2023).

The change in pore pressure at the end of the injection period is reported in Fig. 7(c), while Fig. 7(d) shows the difference in CO_2 saturation at $t = 500$ years for the cases without and with relative permeability hysteresis. Without hysteresis, the CO_2 plume advances several kilometers from the injection point and accumulates at a relative high elevation, forming a gas cap. When relative permeability hysteresis in the gas phase is introduced, however, CO_2 is residually trapped, leading to less mobile CO_2 and a much smaller gas cap (Juanes et al., 2006). The example script also provides visualization tools for several other quantities not shown here.

The number of grid cells in the Johansen model means that the standard direct solver from MATLAB becomes a bottleneck. We can apply techniques from Lie and Møyner (2021), chapter 6 to speed up the simulation. We use the function `getNonLinearSolver` to get reasonable defaults for linear and nonlinear solver and add an override to use the direct solver for comparison purposes. If acceleration is enabled in the script, we also make use of a diagonal AD backend for improved performance.

```
nls = getNonLinearSolver(model, ...
        'TimestepStrategy', 'iteration');
if useAcceleration
model.AutoDiffBackend = ...
DiagonalAutoDiffBackend('useMex', true, ...
        'rowMajor', true);
else
% Override automatic choice
nls.LinearSolver = BackslashSolverAD();
end
```

On a modest laptop, running the simulation that includes hysteresis with a direct solver and the default backend takes 6,857 seconds. If we enable acceleration, the runtime is reduced to 417 seconds. The most significant reduction in runtime comes from the change in linear solver, where using a direct solver takes 6,295 seconds (14 seconds per solve) and the AMGCL-CPR solver uses 181 seconds (or 0.4 seconds per solve). Using the accelerated AD backend reduces the time spent assembling the residual equations and their Jacobian from 522 seconds to 155 seconds. Altogether, the runtime was reduced by almost a factor 40 by making use of a faster AD backend and a better linear solver.

6. Discussion

The three `MRST` extensions presented in this paper provide a starting point for more specific CO_2 storage models using the `ad-blackoil` or `compositional` modules. As discussed next, new contributions may focus on different equations for PVT properties, application of hysteresis to the wetting phase, three-phase systems, or capillary pressure, or mechanical dispersion (Nazari et al., 2024).

6.1 PVT properties

The mixing model presented in Section 2 is based on the formulations by Duan and Sun (2003), Spycher et al. (2003) and Spycher and Pruess (2005). It is most accurate at conditions typical for CGS (i.e., T and P approximately in the intervals $[30, 90]$ °C and $[80, 300]$ bar), and appropriate above the CO_2 critical point (Hassanzadeh et al., 2008). The main focus of Spycher et al. (2003), Spycher and Pruess (2005), and Hassanzadeh et al. (2008) is in predicting the solubility of CO_2 in the aqueous phase (i.e., the mole fraction x_{CO_2}). This is reasonable given the change in aqueous phase properties with CO_2 dissolution, and that x_{CO_2} is a factor two to ten times larger than y_{H_2O} for pressures between 80 and 300 bar and temperatures up to approximately 70 °C. At higher temperatures and $y_{H_2O} \sim x_{CO_2}$ or larger, the assumption of infinite dilution introduces larger error in the calculation of water vaporization (Spycher et al., 2003).

Similarly, if pressure decreases to the point that CO_2 becomes a gas, y_{H_2O} increases much faster, and the assumption no longer applies. (Still, we note that Spycher et al. (2003), indicate good match with experimental data at low pressures.) The error in y_{H_2O} is less than 10% for sodium chloride brines up to 6 molal, and at most 15% for calcium chloride brines up to 3 molal (Spycher and Pruess, 2005). Overall, the implemented PVT model is appropriate for most CO_2 reservoirs in sedimentary basins. In higher temperature and/or salinity reservoirs, or where CO_2 phase changes are expected (as P, T decrease), a different model may be needed. In addition to phase composition, this also applies to errors introduced by some of the PVT property models, such as CO_2 viscosity (Fig. S4, in Supplementary file).

As an alternative to the data-fitted models discussed herein, Xiong et al. (2024) recently introduced a more advanced, but also more computationally expensive, electrolyte cubic plus association (e-CPA) equation of state into `MRST` to better account for the effect of salinity in CCS fluids. Unlike the Spycher model, this predictive model can also account for the solubility of various gases such as methane (CH_4), hydrogen sulfide (H_2S), nitrogen (N_2), oxygen (O_2), and argon (Ar). Consequently, it can be used to simulate a wider variety of CO_2-H_2-salt systems as well as hydrocarbon systems with impure CO_2 injection.

6.2 Relative permeability hysteresis

In Sections 3 and 5, we accounted for relative permeability hysteresis in the nonwetting phase (gas in most sediments), due to its importance during secondary imbibition at the trailing edge of the CO_2 plume (Juanes et al., 2006). Hysteresis in the wetting phase is typically less pronounced (Juanes et al., 2006), but depends on the rock type and fluid system (Naar et al., 1962; Akbarabadi and Piri, 2013). It is well known that the relative permeability of a given fluid phase is impacted by a number of factors including flow rates, pore structure, wettability, and degree of cementation (Naar et al., 1962; Jadhunandan and Morrow, 1995; Spiteri et al., 2008; Krevor et al., 2012). As a result, we emphasize that the choice of the relative permeability model and its parameters must be evaluated on a case-to-case basis, as discussed in more detail in the next paragraph.

Reservoir simulators typically use the models by Killough (1976) or Carlson (1981) to account for relative permeability hysteresis of the nonwetting-phase in two-phase systems (Section 3). In water-wet brine-gas systems, the trapped gas saturation at flow reversal (S_{gt}) determines the amount of residual trapping. In Killough's and most other two-phase hysteretic models, S_{gt} is computed following Land (1968). However, Pentland et al. (2010) showed that, in unconsolidated media, S_{gt} is best approximated by the Aissaoui (1983) and Spiteri et al. (2008) models. If we consider Carlson's model, the scanning curves (and S_{gt}) are obtained by horizontally shifting the bounding imbibition curve. As described in more detail by Spiteri et al. (2008), this is adequate when the scanning curves are near-parallel and have small curvature. Otherwise, negative S_{gt} (nonphysical) may be obtained. Finally, we note that most two-phase hysteretic models, including Killough's and Carlson's, assume reversibility of scanning curves, but this is not supported experimentally (Spiteri and Juanes, 2006 and references therein). Other trapping and relative permeability hysteresis models have been reviewed by Spiteri and Juanes (2006), Spiteri et al. (2008), Pentland et al. (2010), and Beygi et al. (2015).

Our implementation of relative permeability hysteresis in Section 3 targets two-phase water-gas (immiscible) or oil-gas (miscible) systems. Most reservoir simulators model three-phase relative permeability based on the models by Stone (1970, 1973), which assume the following saturation dependencies: $k_{rw}(S_w)$, $k_{rg}(S_g)$, and $k_{ro}(S_w, S_g)$ (Lie, 2019). If the two-phase relative permeabilities display hysteresis, the interpolation method for k_{ro} can also accommodate hysteresis. However, three-phase relative permeability measurement and modeling remain topics of active research (Blunt, 2017), and an in-depth discussion on this topic is beyond the scope of this paper. Therefore, we note that a complete implementation for three-phase fluid systems should also account for hysteresis in the water-oil system, but we do not address this topic further. Interested readers are referred to Spiteri and Juanes (2006), Blunt (2017), Jia et al. (2018), and references therein.

6.3 Diffusion-dispersion

In Section 4, we presented a model for the diffusive flux based on a scalar diffusion coefficient. Besides practicality, the reasoning behind the choice of Eq. (15) is that D_α^γ can be increased to account for mechanical dispersion in relatively homogeneous media (Riaz et al., 2006). However, Saló-Salgado et al. (2024) recently reported that using a scalar coefficient in this model may lead to inaccuracies at higher flow velocities. This is consistent with the findings of Liang et al. (2018), who showed that, in homogeneous glass beads, the dominant mechanism can be estimated as the ratio $\mathscr{D}_\alpha^\gamma/\alpha_t u$, where α_t is the transverse dispersivity (L). This leads to dispersion dominating over molecular diffusion when this ratio is $\ll 1$, which occurs when grain diameters exceed 0.4 mm. In natural sediments, heterogeneity increases the effective dispersivity, which in turn increases mechanical dispersion (Liang et al., 2018). Therefore, our model is appropriate for relatively homogeneous sediments in which molecular diffusion dominates. In heterogeneous media or where larger flow velocities are expected, a dispersion tensor ($\mathbf{D}_{\alpha,h}^\gamma$) is likely necessary.

7. Summary

This work focuses on enhancing the capabilities of the `ad-blackoil` module in `MRST`, with the main goal of simulating 3D geologic carbon dioxide sequestration in saline aquifers. Our contributions, released in the `co2lab-mit` module, can be divided in four sections:

1) Section 2: Thermodynamic model to calculate input PVT properties
2) Section 3: Relative permeability hysteresis
3) Section 4: Molecular diffusion
4) Section 5: Practical usage of the module and computational performance

We provide the code and examples detailing how to use each of these additions, which are intended for models obtained with the `GenericBlackOilModel` class. The description provided in this paper, together with the code, should facilitate implementation of alternative models.

Acknowledgements

L. S. thanks Hassan Hassanzadeh for helpful comments on the calculation of brine-CO_2 PVT properties. This work was supported by ExxonMobil through the project "Modeling and Mitigation of Induced Seismicity and Fault Leakage during CO_2 storage". L. S. thanks The MathWorks, Inc., and the Massachusetts Institute of Technology School of Engineering for funding through a 2020-2021 MathWorks Engineering Fellowship. L. S. gratefully acknowledges the support of a fellowship from "la Caixa" Foundation (No. 100010434). The fellowship code is LCF/BQ/EU21/11890139.

Supplementary file

https://doi.org/10.46690/ager.2024.10.06

Conflict of interest

The authors declare no competing interest.

References

Aissaoui, A. Etude théorique et expérimentale de l'hystérésis des pressions capillaires et des perméabilités relatives en vue du stockage souterrain de gaz. Ecole des Mines de Paris, Paris, 1983. (in French)

Akbarabadi, M., Piri, M. Relative permeability hysteresis and capillary trapping characteristics of supercritical CO_2/brine systems: An experimental study at reservoir conditions. Advances in Water Resources, 2013, 52: 190-206.

Al-Rawajfeh, A. E. Modelling and simulation of CO_2 release in multiple effect distillers for seawater desalination. Halle (Saale), Martin Luther University Halle-Wittenberg, 2004.

Awad, M. M., Espinoza, D. N. Mudrock wettability at pressure and temperature conditions for CO_2 geological storage. International Journal of Greenhouse Gas Control, 2024, 135: 104160.

Aziz, K., Settari, A. Petroleum Reservoir Simulation. London, UK, Applied Science Publishers, 1979.

Batzle, M., Wang, Z. Seismic properties of pore fluids. Geophysics, 1992, 57(11): 1396-1408.

Bear, J. Dynamics of Fluids in Porous Media. New York, USA, Dover, 1972.

Bear, J. Modeling Phenomena of Flow and Transport in Porous Media. Cham, Switzerland, Springer, 2018.

Benson, S., Cook, P., Anderson, J., et al. Underground geological storage, in IPCC Special Report on Carbon Dioxide Capture and Storage, edited by B. Metz, O. Davidson, H. de Coninck, et al. Cambridge University Press, Cambridge, pp. 196-276, 2005.

Beygi, M. R., Delshad, M., Pudugramam, V. S., et al. Novel three-phase compositional relative permeability and three-phase hysteresis models. SPE Journal, 2015, 20(1): 21-34.

Blunt M. J. Multiphase Flow in Permeable Media: A Pore-scale Perspective. Cambridge, UK, Cambridge University Press, 2017.

Boait, F. C., White, N. J., Bickle, M. J., et al. Spatial and temporal evolution of injected CO_2 at the Sleipner Field, North Sea. Journal of Geophysical Research: Solid Earth, 2012, 117(B3): B03309.

Carlson, F. M. Simulation of relative permeability hysteresis to the nonwetting phase. Paper SPE 10157 Presented at the SPE Annual Technical Conference and Exhibition, San Antonio, Texas, 4-7 October, 1981.

Davidson, T. A. A simple and accurate method for calculating viscosity of gaseous mixtures. Washington, Bureau of Mines, US Department of the Interior, 1993.

Duan, Z., Sun, S. An improved model calculating CO_2 solubility in pure water and aqueous NaCl solutions from 273 to 533 K and from 0 to 2000 bar. Chemical Geology, 2003, 193(3-4): 257-271.

Eikehaug, K., Haugen, M., Folkvord, O., et al. Engineering meter-scale porous media flow experiments for quantitative studies of geological carbon sequestration. Transport in Porous Media, 2024, 151: 1143-1167.

Fenghour, A., Wakeham, W. A., Vesovic, V. The viscosity of carbon dioxide. Journal of Physical and Chemical Reference Data, 1998, 27(1): 31-44.

Fernø, M. A., Haugen, M., Eikehaug, K., et al. Room-scale CO_2 injections in a physical reservoir model with faults. Transport in Porous Media, 2024, 151: 913-937.

Fick, A. V. On liquid diffusion. The London, Edinburgh, and Dublin Philosophical Magazine and Journal of Science, 1855, 10(63): 30-39.

Flemisch, B., Nordbotten, J. M., Fernø, M., et al. The FluidFlower validation benchmark study for the storage of CO_2. Transport in Porous Media, 2024, 151: 865-912.

Garcia, J. E. Density of aqueous solutions of CO_2. Berkeley, Lawrence Berkeley National Laboratory, 2001.

Gasda, S. E., Nordbotten, J. M., Celia, M. A. Vertically averaged approaches for CO_2 migration with solubility trapping. Water Resources Research, 2011, 47(5): W05528.

Hassanzadeh, H., Pooladi-Darvish, M., Elsharkawy, A. M., et al. Predicting PVT data for CO_2-brine mixtures for black-oil simulation of CO_2 geological storage. International Journal of Greenhouse Gas Control, 2008, 2(1): 65-77.

Haugen, M., Saló-Salgado, L., Eikehaug, K., et al. Physical variability in meter-scale laboratory CO_2 injections in faulted geometries. Transport in Porous Media, 2024, 151: 1169-1197.

Hebach, A., Oberhof, A., Dahmen, N. Density of water + carbon dioxide at elevated pressures: measurements and correlation. Journal of Chemical & Engineering Data, 2004, 49(4): 950-953.

Hesse, M. A., Woods, A. W. Buoyant dispersal of CO_2 during geological storage. Geophysical Research Letters, 2010, 37(1): L01403.

Hidalgo, J. J., Carrera, J. Effect of dispersion on the onset of convection during CO_2 sequestration. Journal of Fluid Mechanics, 2009, 640: 441-452.

Islam, A. W., Carlson, E. S. Viscosity models and effects of dissolved CO_2. Energy & Fuels, 2012, 26(8): 5330-5336.

Jadhunandan, P. P., Morrow, N. R. Effect of wettability on waterflood recovery for crude-oil/brine/rock systems. SPE Reservoir Engineering, 1995, 10(1): 40-46.

Jia, W., McPherson, B., Pan, F., et al. Impact of three-phase relative permeability and hysteresis models on forecasts of storage associated with CO_2-EOR. Water Resources Research, 2018, 54(2): 1109-1126.

Juanes, R., Spiteri, E. J., Orr Jr F. M., et al. Impact of relative permeability hysteresis on geological CO_2 storage. Water Resources Research, 2006, 42(12): W12418.

Killough, J. E. Reservoir simulation with history-dependent saturation functions. Society of Petroleum Engineers Journal, 1976, 16(1): 37-48.

King, M. B., Mubarak, A., Kim, J. D., et al. The mutual solubilities of water with supercritical and liquid carbon dioxides. The Journal of Supercritical Fluids, 1992, 5(4): 296-302.

Krevor, S., De Coninck, H., Gasda, S. E., et al. Subsurface carbon dioxide and hydrogen storage for a sustainable energy future. Nature Reviews Earth & Environment, 2023, 4: 102-118.

Krevor, S. C. M., Pini, R., Zuo, L., et al. Relative permeability and trapping of CO_2 and water in sandstone rocks at reservoir conditions. Water Resources Research, 2012, 48(2): W02532.

Land, C. S. Calculation of imbibition relative permeability for two-and three-phase flow from rock properties. Society of Petroleum Engineers Journal, 1968, 8(2): 149-156.

Landa-Marbán, D., Tveit, S., Kumar, K., et al. Practical approaches to study microbially induced calcite precipitation at the field scale. International Journal of Greenhouse Gas Control, 2021, 106: 103256.

Liang, Y., Wen, B., Hesse, M. A., et al. Effect of dispersion on solutal convection in porous media. Geophysical Research Letters, 2018, 45(18): 9690-9698.

Lie, K. -A. An Introduction to Reservoir Simulation Using MATLAB/GNU Octave: User Guide for the MATLAB Reservoir Simulation Toolbox (`MRST`). Cambridge, UK, Cambridge University Press, 2019.

Lie, K. -A., Møyner, O. Advanced Modeling with the MATLAB Reservoir Simulation Toolbox. Cambridge, UK, Cambridge University Press, 2021.

Muskat, M. Physical Principles of Oil Production. New York, USA, McGraw-Hill Book Co, 1949.

Møyner, O., Andersen, O., Nilsen, H. M. Multi-model hybrid compositional simulator with application to segregated flow. Computational Geosciences, 2020, 24(2): 775-787.

Møyner, O., Nilsen, H. M. Multiresolution coupled vertical equilibrium model for fast flexible simulation of CO_2 storage. Computational Geosciences, 2019, 23(1): 1-20.

Naar, J., Wygal, R. J., Henderson, J. H. Imbibition relative permeability in unconsolidated porous media. Society of Petroleum Engineers Journal, 1962, 2(1): 13-17.

Nazari, F., Nafchi, S. A., Asbaghi, E. V., et al. Impact of capillary pressure hysteresis and injection-withdrawal schemes on performance of underground hydrogen storage. International Journal of Hydrogen Energy, 2024, 50: 1263-1280.

Neufeld, J. A., Hesse, M. A., Riaz, A., et al. Convective dissolution of carbon dioxide in saline aquifers. Geophysical research letters, 2010, 37(22): L22404.

Nilsen, H. M., Lie, K. -A., Andersen, O. Robust simulation of sharp-interface models for fast estimation of CO_2 trapping capacity in large-scale aquifer systems. Computational Geosciences, 2016, 20: 93-113.

Nilsen, H. M., Lie, K. -A., Møyner, O., et al. Spill-point analysis and structural trapping capacity in saline aquifers using MRST-co2lab. Computers & Geosciences, 2015, 75: 33-43.

Nordbotten, J. M., Ferno, M. A., Flemisch, B., et al. The 11th Society of Petroleum Engineers Comparative Solution

Project: Problem Definition. SPE Journal, 2024, 29(5): 2507-2524.

Pentland, C. H., Itsekiri, E., Al Mansoori, S. K., et al. Measurement of nonwetting-phase trapping in sandpacks. SPE Journal, 2010, 15(2): 274-281.

Redlich, O., Kwong, J. N. S. On the thermodynamics of solutions. V. An equation of state. Fugacities of gaseous solutions. Chemical Reviews, 1949, 44(1): 233-244.

Riaz, A., Hesse, M., Tchelepi, H. A., et al. Onset of convection in a gravitationally unstable diffusive boundary layer in porous media. Journal of Fluid Mechanics, 2006, 548: 87-111.

Rowe Jr, A. M., Chou, J. C. S. Pressure-volume-temperature-concentration relation of aqueous sodium chloride solutions. Journal of Chemical and Engineering Data, 1970, 15(1): 61-66.

Saadatpoor, E., Bryant, S. L., Sepehrnoori, K. New trapping mechanism in carbon sequestration. Transport in Porous Media, 2010, 82(1): 3-17.

Saló-Salgado, L., Haugen, M., Eikehaug, K., et al. Direct comparison of numerical simulations and experiments of CO_2 injection and migration in geologic media: Value of local data and forecasting capability. Transport in Porous Media, 2024, 151: 1199-1240.

Silva, J. A., Saló-Salgado, L., Patterson, J., et al. Assessing the viability of CO_2 storage in offshore formations of the Gulf of Mexico at a scale relevant for climate-change mitigation. International Journal of Greenhouse Gas Control, 2023, 126: 103884.

SLB. ECLIPSE Reference Manual. Houston, USA, Schlumberger Ltd., 2014a.

SLB. ECLIPSE Technical Description. Houston, USA, Schlumberger Ltd., 2014b.

Spiteri, E. J., Juanes, R. Impact of relative permeability hysteresis on the numerical simulation of WAG injection. Journal of Petroleum Science and Engineering, 2006, 50(2): 115-139.

Spiteri, E. J., Juanes, R., Blunt, M. J., et al. A new model of trapping and relative permeability hysteresis for all wettability characteristics. SPE Journal, 2008, 13(3): 277-288.

Spycher, N., Pruess, K. CO_2-H_2O mixtures in the geological sequestration of CO_2. II. Partitioning in chloride brines at 12-100 °C and up to 600 bar. Geochimica et Cosmochimica Acta, 2005, 69(13): 3309-3320.

Spycher, N., Pruess, K., Ennis-King, J. CO_2-H_2O mixtures in the geological sequestration of CO_2. I. Assessment and calculation of mutual solubilities from 12 to 100 °C and up to 600 bar. Geochimica et Cosmochimica Acta, 2003, 67(16): 3015-3031.

Stone, H. L. Probability model for estimating three-phase relative permeability. Journal of Petroleum Technology, 1970, 22(2): 214-218.

Stone, H. L. Estimation of three-phase relative permeability and residual oil data. Journal of Canadian Petroleum Technology, 1973, 12(4): 53-61.

Szulczewski, M. L., MacMinn, C. W., Herzog, H. J., et al. Lifetime of carbon capture and storage as a climate-change mitigation technology. Proceedings of the National Academy of Sciences, 2012, 109(14): 5185-5189.

Wang, Y., Fernàndez-Garcia, D., Saaltink, M. W. Modeling reactive multi-component multi-phase flow for Geological Carbon Sequestration (GCS) with Matlab. Computers & Geosciences, 2023, 172: 105300.

Xiong, W., Zhang, L., Zhao, Y., et al. Compositional simulation for carbon storage in porous media using an electrolyte association equation of state. SPE Journal, 2024, 29(6): 3314-3336.